Organic Geochemistry 200 (2025) 104882

Contents lists available at ScienceDirect

Organic Geochemistry

journal homepage: www.elsevier.com/locate/orggeochem

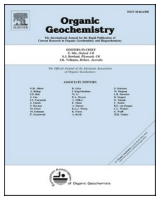

Constraining the sources of archaeal tetraether lipids in multiple cold seep provinces of the Cascadia Margin

Katherine J. Keller [a,*], Mark M. Baum [b], Xiao-Lei Liu [c], Kemi Ashing-Giwa [a,d], Isabel R. Baker [a,e], Jerome Blewett [a], Ann Pearson [a]

[a] Harvard University, Department of Earth and Planetary Sciences, USA
[b] Unaffiliated
[c] School of Geosciences, University of Oklahoma, USA
[d] Doer School of Sustainability, Stanford University, USA
[e] Johns Hopkins University, Department of Earth and Planetary Sciences, USA

ARTICLE INFO

Associate editor – Cindy de Jonge

Keywords:
Isoprenoid GDGTs
Carbon isotopes
Methane cycling

ABSTRACT

Archaeal isoprenoid glycerol dialkyl glycerol tetraether lipid (iGDGT) abundance profiles and carbon isotopic compositions reflect the relative distributions of archaeal sources, including planktonic, benthic, and methane-cycling contributions. Here, we analyze the carbon isotope ratios of iGDGTs purified from sediments of three different cold seep sites in Cascadia Margin, off the coast of Washington, USA. Together with relative abundance and glycerol configurations, we use the carbon isotope ratios to estimate the contributions of multiple archaeal sources to the sedimentary iGDGT assemblages and their impact on values of the TEX_{86} and methane indices. Using a Bayesian mixing model, we robustly characterize three potential endmembers by determining their characteristic lipid distributions, inferred contributions to the total sediment inventory, and carbon isotopic signatures. Despite the geographic proximity of the sample locations, we find site-specific heterogeneity in relative iGDGT abundances and $\delta^{13}C$ values. Planktonic and benthic methane-cycling sources predominate in all cases (contributing > 98% of iGDGTs), while benthic non-methane cycling archaea contribute minimally to the sedimentary lipid pool. Environments with higher methane influence show an increased presence of anti-parallel iGDGTs, indicating that methane-cycling archaea may dominantly or exclusively synthesize iGDGTs in this configuration. Our results quantify the relationship between the methane index (MI) and methane impact in systems dominated by planktonic and benthic methane-cycling archaea. Within the framework of the TEX_{86} temperature proxy, this permits a quantitative demonstration that it is overly simplistic to apply a MI cutoff threshold as a binary indicator to determine methane influence, and caution is needed when taking this approach in paleoclimate reconstructions.

1. Introduction

Due to their ubiquity and high preservation potential, archaeal iGDGTs have been used extensively to reconstruct past sea-surface temperatures (SSTs) and to investigate marine carbon cycling and greenhouse climates (Jenkyns et al., 2012; Ho and Laepple, 2016; Brien et al., 2017; Elling et al., 2019). The TEX_{86}-SST proxy, based on the relative ratio of cyclized iGDGTs (Schouten et al., 2013; Tierney, 2014), relies on the assumption that iGDGTs recovered from marine sediments originate solely or in great majority from the planktonic, ammonia oxidizing *Nitrososphaerota* (*syn.* Thaumarchaeota). Nevertheless, the extent to which other sources, such as allochthonous input from rivers or soils and in-situ benthic production, contribute to the sedimentary lipid pool remains largely uncertain (Pearson and Ingalls, 2013). Significant inputs from these sources can have notable implications for the practical use and interpretation of the TEX_{86}-SST proxy (Besseling et al., 2018, 2020; Biddle et al., 2006; Lincoln et al., 2014; Liu et al., 2011; Pearson et al., 2016; Shah et al., 2008), but the formulation of TEX_{86} as a ratio of sums suppresses its sensitivity to heterogeneous signals, including changes in ring-bearing iGDGTs that appear in both the numerator and denominator, e.g., iGDGT-2 and -3 (Taylor et al., 2013, Rattanasriampaipong et al., 2022). Particularly in cases with exogenous

* Corresponding author.
E-mail address: katherinekeller@g.harvard.edu (K.J. Keller).

https://doi.org/10.1016/j.orggeochem.2024.104882
Received 17 August 2024; Received in revised form 2 October 2024; Accepted 2 October 2024
Available online 4 October 2024

sources from compositionally similar material, this requires other methods to identify contributions of iGDGTs and their origins (Pearson et al., 2016).

To date, several metrics have been developed to qualitatively indicate the presence of secondary inputs. Impacts from methane-cycling archaea can be indicated using the Methane Index (MI), which is based on characteristic production of specific cyclized iGDGTs (Zhang et al., 2011, 2016; Kim and Zhang, 2023); environments characterized by anaerobic oxidation of methane (AOM), such as continental shelves and methane seeps, tend to exhibit elevated MI values. However, methanotrophic influences vary spatially and temporally, and universal thresholds to identify non-marine iGDGT assemblages are uncertain. For instance, elevated MI values may not always indicate AOM and, conversely, low values might overlook the presence of slow-growing archaeal contributions or small diffusive fluxes of methane (Polik et al., 2018; Kim and Zhang, 2023). Further, using iGDGT relative abundances to distinguish allochthonous inputs is complicated by unknown identities and/or metabolic pathways of the potential source organisms and does not provide quantitative estimates of heterogeneous inputs (Pancost et al., 2001; Biddle et al., 2006; Kellermann et al., 2012; Yoshinaga et al., 2015; Blewett et al., 2022). Accompanying these index-based methods with supplementary diagnostic tools should allow for a more robust approach to probe the degree of sedimentary overprinting.

The carbon isotope composition of iGDGTs ($\delta^{13}C$) offers an additional means to constrain exogenous inputs (Zhu et al., 2021). Recent work on iGDGTs and bacterial branched GDGTs in wetlands and the modern and Paleocene Arctic indicate that different carbon sources and metabolisms impart distinct $\delta^{13}C$ signatures (Elling et al., 2019; Lattaud et al., 2021; Blewett et al., 2022). In methane-rich environments, diagnostic biphytane and archaeol lipid biomarkers of anaerobic methane-cycling archaea (ANME) provide evidence of methane oxidation in marine sediments (Hinrichs et al., 1999; Pancost et al., 2001; Elvert et al., 2005; Stadnitskaia et al., 2008). The incorporation of ^{13}C-depleted dissolved inorganic carbon (DIC), derived from methane oxidation, into the lipid biomass results in a characteristic isotopic signature observed in both intact iGDGTs and their biphytane derivatives (Kellermann et al., 2012). This facilitates the disentanglement of source contributions using distinct $\delta^{13}C$ values, particularly when these values correspond to well-characterized endmembers. Further, chemical degradation and analysis of the molecular structures of iGDGT isomers shows that different archaeal communities synthesize unique glycerol configurations (parallel or anti-parallel arrangement of glycerol moieties; Liu et al., 2018, 2019). These works indicate that iGDGTs recovered from AOM environments are predominantly in the anti-parallel configuration, compared to mostly parallel configurations found in pelagic, marine settings. Together, these tools can be used to differentiate between mixed benthic *in situ* and planktonic sources.

It is imperative to establish a comprehensive framework for identifying multiple sources of iGDGTs, given the continued significance of archaeal lipids as a tool for understanding past climate systems. Here, we test common estimators used to indicate methane impact by analyzing the iGDGT relative abundances, glycerol arrangements, and $\delta^{13}C$ values of iGDGTs purified from surface sediments collected from cold seep provinces of the Cascadia Margin. We infer the fractional source contributions, $\delta^{13}C$ signatures, and relative iGDGT distributions for each endmember using a probabilistic 3-component Bayesian mixing model.

2. Material and Methods

2.1. Sample Locations

Sediment push cores (8 cm) were obtained by remotely operated vehicle (ROV) SuBastian during the Schmidt Ocean Institute Cruise FK081824 (August-September 2018) in three cold seep provinces, Cascadia Margin: Astoria Canyon (AC), McArthur Canyon (MC), and Hydrate Ridge (HR). Samples were taken near areas of active methane bubble plumes and at radial distances from the plumes (Table 1). Cores were divided into depth intervals of 1 cm (0–4 cm) and 2 cm (4–8 cm) and stored at −20 °C until analysis. The 2–4 cm and 6–8 cm horizons were saved as archival material, and the others were used in this analysis.

2.2. Lipid Extraction and Purification

Sediments were freeze dried and homogenized, followed by lipid extraction using a Microwave-Assisted Extraction System (MARS, CEM corporation) as detailed in earlier works (Pearson et al., 2016). In brief, a 3-step successive extraction method using 1:1 CH_2Cl_2: CH_3OH, 9:1 CH_2Cl_2:CH_3OH, and 100% CH_2Cl_2 mixtures was performed to obtain total lipid extracts (TLE). The extraction method includes a 30 min ramped heating to 70 °C followed by a 20 min hold and cooling to room temperature (Huguet et al., 2006). Approximately 10% of TLEs were archived, 2–5% were aliquoted for analysis of iGDGT distributions, and the remaining TLEs were hydrolyzed in MeOH/HCl (95:5) for 3 h at 70 °C followed by partitioning over SiO_2 (130–270 mesh; Sigma Aldrich) to yield a core iGDGT fraction. Approximately 1 μ g of the archived TLE were used for analysis of iGDGT parallel and anti-parallel arrangement.

Individual iGDGTs were isolated by normal phase chromatography (Agilent NH_2-column, 4.6 × 250 mm, 5 μm, p.n. 880952–708) with isocratic elution using isopropanol/hexane (1.35/98.65) at a flow rate of 1 ml/min. Targeted iGDGTs were collected by time-based fraction collection (for method details, see Pearson et al., 2016) with optimized peak separation to minimize isotope fractionation (Keller et al., 2023). After normal phase collection, iGDGTs were purified from background contamination by reverse phase chromatography (ZORBAX Eclipse XDB-C8 column, 4.6x150 mm, 5 mm, p.n. 993967-906) and a gradient of acetonitrile, water and ethyl acetate, as detailed previously (Ingalls et al., 2006; Shah et al., 2008; Pearson et al., 2016). Concentrations and potential contamination were analyzed using flow injection analysis (FIA) monitoring m/z 300–1300, relative to a dilution series of C_{46}-GTGT standards (Huguet et al., 2006).

2.3. HPLC-ACPI-MS and index calculation

Compound identification and relative iGDGT distributions were conducted via high-performance liquid chromatography coupled with atmospheric pressure chemical ionization (APCI-MS) using an Agilent 6460 series triple quadrupole mass spectrometer, following established protocols (Becker et al., 2015). Prior to analysis, aliquots were dissolved in hexane/isopropanol (99:1, v/v) and filtered using a 0.45 mm PTFE filter.

To detect methane impact, we calculated methane index (Zhang et al., 2011):

$$MI = \frac{[iGDGT-1]+[iGDGT-2]+[iGDGT-3]}{[iGDGT-1]+[iGDGT-2]+[iGDGT-3]+[Cren]+[Cren']}$$

where brackets refer to the percent of the compounds and iGDGT-x refers to the GDGT with x number of cyclopentane rings; [Cren] and [Cren'] refer to crenarchaeol and its late-eluting isomer, respectively (Schouten et al., 2013). We also calculated the TEX_{86} index:

Table 1
Sample location details in this study. *Refers to the radial distance of each sample site from the modern location of measured methane bubbling.

Location	Latitude	Longitude	Water depth (m)	Distance* (m)
Astoria Canyon	46.133°	−124.395°	494	0, 20
McArthur Canyon	45.848°	−124.895°	829, 831	0, 30, 60
Hydrate Ridge	44.570°	−125.148°	788, 797, 800	0, 10, 30, 60

$$TEX_{86} = \frac{[iGDGT-2]+[iGDGT-3]+[Cren']}{[iGDGT-1]+[iGDGT-2]+[iGDGT-3]+[Cren']}$$

Finally, to investigate the influence of sedimentary overprinting on TEX_{86}-derived SST reconstructions, we applied the BAYSPAR calibration to calculate the offset between TEX_{86}-SST and reported annual average SST, denoted as ΔSST (Tierney and Tingley, 2015). The 50th percentile was used for $SST_{observed}$:

$$\Delta SST = SST_{TEX86} - SST_{observed}$$

2.4. Carbon isotope analysis of iGDGTs

Values of $\delta^{13}C$ for purified iGDGT compounds were obtained using Spooling Wire Microcombustion IRMS (Pearson et al., 2016). Data are reported on the Vienna Pee Dee Belemenite scale and were blank-corrected and standardized to the same reference frame using two independent standards–acyclic synthetic iGDGT analog, C_{46}-GTGT (m/z 744, −30.3‰), and an in-house standard, Carolina Margin crenarchaeol (m/z 1292, −18.5‰), previously isolated and purified (Pearson et al., 2016; Hurley et al., 2019). Between 6–8 replicate measurements were performed for each iGDGT sample, and results were averaged; outliers were detected and removed using Q-outlier test (95% confidence interval). After RP-HPLC, we evaluate the purity of each iGDGT by FIA and assign it a purity score. This score, calculated using an empirical formula that converts between molecular ion abundance and total ion abundance (Pearson et al., 2016), represents the fraction of the TIC signal that is assigned to a specific iGDGT. Low purity scores (<0.85) reflect the co-elution and collection of other GDGT compounds (e.g. iGDGT-4 in the crenarchaeol fraction).

2.5. Glycerol configuration analysis

Chemical degradation and structural isomer analysis was performed at the University of Oklahoma with reverse phase liquid chromatography coupled to an Agilent 6530 QTOF mass spectrometer through an Agilent jet stream dual electrospray ionization (AJS-ESI) interface; analytical protocols followed Liu et al. (2018, 2019). To interpret the relative proportions of parallel and antiparallel iGDGTs in each sample, we calculated a ratio of relevant compounds, namely biphytanediols (bpdiol), monoallyl biphytanol monoethers (mbpm), and diallyl biphytanyl diethers (dbpd), as described in Liu et al., 2019:

$$Isomer\ Ratio = \frac{[mbpm]}{[bpdiol]+[dbpd]}$$

2.6. Bayesian mixing model

We constructed a Bayesian mixing model to infer contributions from three primary endmembers: planktonic (100% autotrophic, presumed analogous to the model taxon *Nitrosopumilus maritimus*; Könneke et al., 2005), benthic methane-cycling, and benthic non-methane-cycling. Notably, we assume that the benthic methane-cycling endmember includes both methanotrophic and methanogenic archaea. The model results provide estimates for the iGDGT profiles (X) and the relative proportions of each endmember (F), as well as the endmember mean $\delta^{13}C$ value. Estimates of X also yield values for MI and TEX_{86}. The model implements a series of algebraic relationships which incorporate $\delta^{13}C$ values of iGDGTs and relative abundances measured across coring locations and sampling depth horizons; the inferred parameters are an integrated representation of all observations. We obtained 259 measurements of iGDGT relative abundance and 122 compound-specific $\delta^{13}C$ measurements. Samples lacking $\delta^{13}C$ iGDGT measurements were excluded from the analysis. For any given sample (i), the model evaluates the contribution from each endmember source (k), and the relative distribution within that source (j), as follows:

$$M_i = \sum F_{i,k} X_{k,j}$$

and

$$\delta^{13}C_i = \sum F_{i,k} X_{k,j}\ \delta_k / M_i$$

M_i and $\delta^{13}C_i$ are deterministic functions of X and F, and δ refers to the $\delta^{13}C$ values of the end-member source. The model employs broad ranges of isotopic endmember and relative abundance parameters for the priors, as detailed in Table 2. The model is conditioned on observed values for M and $\delta^{13}C$, inferring the parameters F and X. All data are used simultaneously, across all cold-seep locations and sampling depths, using the following likelihood functions:

$$M_i\ TruncatedNormal\left(u = M_i^{predicted}, \sigma = \sigma_{Mi}\right)$$

$$\delta^{13}C_k\ Normal\left(u = C_i^{predicted}, \sigma = \sigma_{\delta^{13}Ci,k}\right)$$

Here, the truncated Normal distribution ensures that values are between 0 and 1. The prior distributions for, $X_{i,j}$ and F_i, are modeled as follows:

$$X_{i,k}\ Beta\left(u_{i,k}, \Sigma_{i,k}\right)$$

$$F_i\ Dirichilet(\alpha_k)$$

Upper and lower bounds are used to parameterize the mean and standard deviation of the Beta distribution, constrained to between 0 and 1 (Table 2). A Dirichlet distribution is used to ensure that all fractional contributions of each endmember of F_i sum to 1. For each location, the prior for F_i is uniform on the simplex, with alpha values equal to 1. Incorporating the full set of observations, the model provides samples from the posterior distribution using a Markov Chain Monte Carlo simulation using python PyMC package. We validated the model structure using a test model with known values for X and F to ensure correct parameter estimations (see Supplemental Material, Sections S3, S4). Summary of the parameters, distributions and notation used in the model can be found in Tables S1 and S2.

3. Results

3.1. Lipid distributions and iGDGT $\delta^{13}C$ values

3.1.1. McArthur Canyon (MC)

At MC, the relative abundance of iGDGT-0 is high compared to minor iGDGTs (iGDGT-1, -2, and -3) and crenarchaeol (Fig. 1), consistent with distribution patterns associated with cold marine environments (Zhang et al., 2011). Even in the core collected from an area experiencing active methane bubbling, only minor increases in iGDGT-1 and -2 abundances (typically associated with ANME sources) were observed. The relative abundances of iGDGT-1 and -2 were minimal (between 0.03 and 0.08 fractional abundance) and abundances of iGDGT-3 and -4 were even smaller, ranging from < 0.005 to 0.01 across all sample depths.

The range of $\delta^{13}C$ values for MC was relatively narrow, with iGDGT-0 and crenarchaeol varying from −21.7 to −18.9‰. Due to the low abundance of minor iGDGT compounds, i.e., not reaching the analytical threshold required for SWiM analysis, only a few $\delta^{13}C$ measurements of iGDGT-1 and -2 were obtained. Among those samples, the values were generally more negative than the associated iGDGT-0 and crenarchaeol, with the greatest ^{13}C-depletion observed for sediments closest to the active methane seep (−29.2 and −44.5‰ for iGDGT-1 and -2, respectively; Fig. 2). The majority of the minor iGDGT samples for MC had low purity scores (<0.85) which indicates co-elution of other compounds during HPLC separation.

Table 2
Estimated ranges for relative abundances and $\delta^{13}C$ values used to develop priors for iGDGT distributions for each endmember ; [b]Pohlman et al., 2011; [c]Biddle et al., 2006

Source	iGDGT-0	iGDGT-1	iGDGT-2	iGDGT-3	iGDGT-4	Cren	iGDGT-5	$\delta^{13}C$ (‰)
Planktonic	0.2–0.8	0.0–0.2	0.0–0.1	0.0–0.05	0.0	0.2–0.5	0.0—–0.05	−22 to −18[a]
Benthic/ methane-cycling	0.2–0.5	0.05–0.2	0.2–0.5	0.05–0.2	0.0–0.1	0.0	0.0	−120 to −40[b]
Benthic/ non-methane cycling	0.1–0.5	0.0–0.3	0.0–0.3	0.0–0.3	0.0–0.3	0.0	0.0–0.1	−30 to −22[c]

Source (i.e., $X_{j,k}$–see methods). Estimated distributions were based on iGDGT profiles from previous works (see Supplemental Material); references are given for $\delta^{13}C$ endmember ranges. Larger ranges indicate less certainty. [a]Hurley et al., 2019.

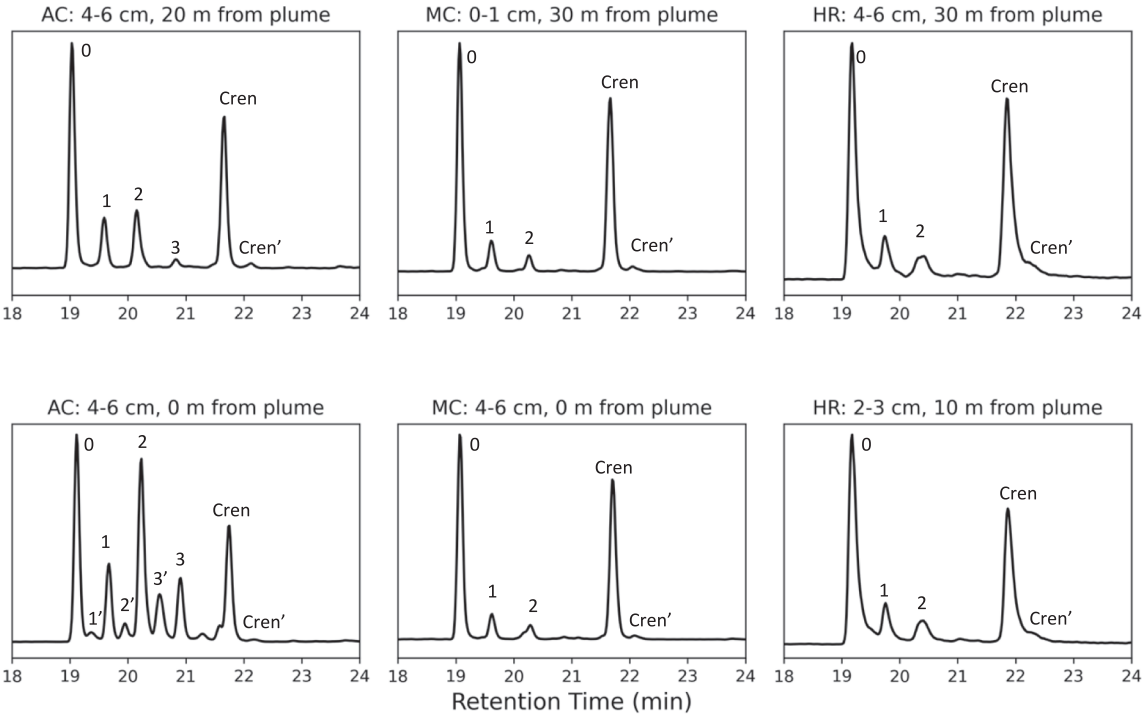

Fig. 1. HPLC-APCI-MS total ion chromatograms displaying example core iGDGT profiles from each location with representative distances from the methane plume. AC, MC, and HR refer to Astoria Canyon, McArthur Canyon, and Hydrate Ridge, respectively. The specific iGDGTs are labeled by the number of internal cyclopentane rings. Early-eluting iGDGT isomers (‘ symbol) are not fully resolved from main peaks, and are collected together with main peaks for $\delta^{13}C$ analysis to avoid ^{13}C fractionation due to incomplete/partial peak collection (Keller et al., 2023).

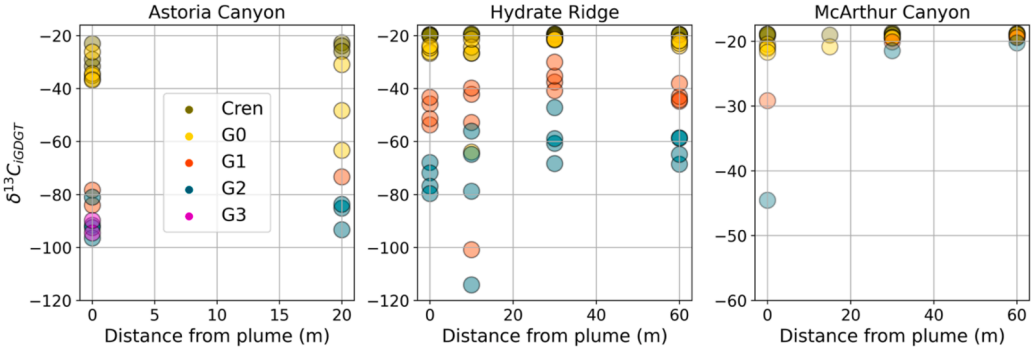

Fig. 2. Compound-specific $\delta^{13}C$ values for each individual sampling location and depth. The core iGDGT structures are abbreviated as G0, G1, G2, G3, with the numbers denoting internal cyclopentane rings.

3.1.2. Hydrate Ridge (HR)

Samples from HR exhibit similar iGDGT distribution patterns to those observed at MC, but with greater abundances of iGDGT-1 and -2. Profile patterns were generally alike between samples despite varying distances from the bubble plume and different depth intervals (Fig. 1). The majority of core iGDGTs were comprised of iGDGT-0 and crenarchaeol. Notably, one sample (S43) revealed anomalously higher iGDGT-1 and -2 abundances (0.17 and 0.26 fractional abundance, respectively) compared to typical abundances of *ca.* 0.10 observed for those compounds. HR samples reveal slightly more heterogeneous $\delta^{13}C$ values compared to MC samples (Fig. 2). The most ^{13}C-depleted compounds measured were iGDGT-1 and –2, with $\delta^{13}C$ values generally

ranging between *ca.* −50 to −30‰ and −114 to −50‰, respectively. Like MC, many iGDGT-1 samples have low purity scores (< 0.85) which may contribute to the large range of values seen across these compounds; however, high purity scores are observed for the majority of iGDGT-2 samples, which have an even broader range of observed $\delta^{13}C$ values. This points toward multiple archaeal sources contributing to the total iGDGT lipid pool rather than to any effect of co-eluting compounds. A small $\delta^{13}C$ range was observed for iGDGT-0 and crenarchaeol across all sample depths and distances from the modern methane plume. Generally, a $\delta^{13}C$ range of −26.9‰ to −20.8‰ was observed for iGDGT–0, and an even narrower range was observed for crenarchaeol, with $\delta^{13}C$ values ranging between −20.1‰ and –19.3‰. A single outlier, sample S43, exhibits $\delta^{13}C$ values of −64.0‰ and −26.4‰ for iGDGT-0 and crenarchaeol, respectively.

3.1.3. Astoria canyon (AC)

AC samples reveal distinct iGDGT distribution patterns and isotopic ratios compared to the other sites (Fig. 1). The samples showcase canonical distribution patterns associated with methane influence (Zhang et al., 2011). Minor iGDGTs, particularly iGDGT-2, make up a considerably larger fraction of the recovered core iGDGTs compared to the other sites. Relative abundances of iGDGT-2 range from 0.13 to 0.28, and iGDGT-3 (with multiple early-eluting iGDGT isomer compounds) also is relatively more abundant (0.11–0.16), whereas iGDGT-3 was virtually absent at the other sites.

The largest range of $\delta^{13}C$ values for iGDGTs is observed at AC (Fig. 2). Unlike MC and HR samples, $\delta^{13}C$ values of iGDGT-0 are highly heterogeneous, ranging from *ca.* −60 to −25‰, whereas $\delta^{13}C$ values measured for iGDGT-1, -2, and -3 generally converge between −100 and −80‰. A larger spread of values is observed for samples collected farther from the methane plume (20 m) compared to those taken directly from the detected bubbling, which may point toward a more heterogeneous mix of archaeal sources at distance. The $\delta^{13}C$ values of crenarchaeol fractions are anomalously ^{13}C-depleted at AC, varying from −22.7‰ to −36.4‰; the most negative values are observed closest to the plume. Notably, the low $\delta^{13}C$ value crenarchaeol samples also have low purity scores (Figs. 3 and 4), suggesting co-elution of other (non-crenarchaeol) compounds during HPLC, consistent with the general inability to separate crenarchaeol from iGDGT-4 in normal phase HPLC.

3.2. Calculated methane index

Higher calculated MI values are observed in locations with lower $\delta^{13}C$ iGDGT values (Fig. 3). AC and HR demonstrate a spectrum of MI values, with HR having a range of about 0.20 to 0.35 (S43 being an outlier) and AC having an even broader range of about 0.45 to 0.80. Consistently low MI values are observed at MC, with values hovering near 0.20. The lowest MI values occur furthest from the methane plume at MC, although the spread of MI values across sample locations and depth intervals is small (0.20 to 0.23). Notably, only one sample from HR (S43) but all samples from AC have MI values above 0.45.

3.3. Chemical degradation products

Selective *sn*2 ether bond cleavage of iGDGTs with parallel glycerol configuration yields two distinct degradation products, bpdiol and dbpd, whereas cleavage of antiparallel iGDGTs yields two mbpm (Fig. S1). The isomer ratio provides a metric for the relative proportion of antiparallel and parallel iGDGTs in each sample; higher ratios indicate a larger proportion of iGDGTs in the antiparallel–i.e., presumed non-planktonic–configuration (Liu et al., 2019). Similar to the MI results, sediments from MC had the lowest isomer ratios, with values < 0.05 for most samples. Intermediate proportions of antiparallel structures were observed for HR, with values generally falling between 0.05 and 0.15, although sample S43 exhibits an anomalously high isomer ratio value. The highest relative proportions of antiparallel structures (0.28 to 0.84) were detected for samples from AC, where the extremely ^{13}C-depleted signatures also were observed. Overall, there appears to be a broad positive correlation between isomer ratios and ^{13}C-depletion of iGDGTs (Figs. 3 and 4), consistent with previous conclusions (Liu et al., 2019).

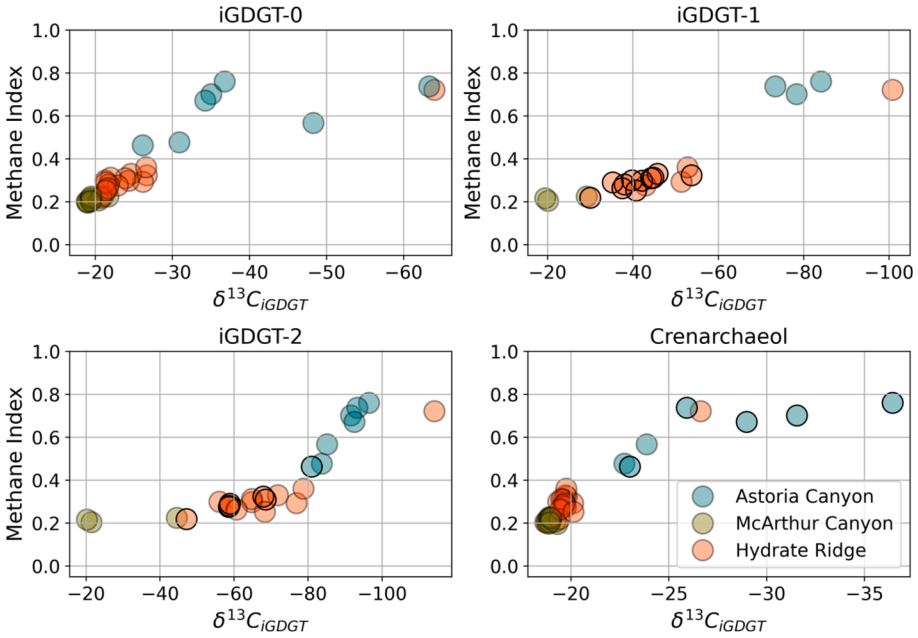

Fig. 3. The methane index relative to the $\delta^{13}C$ composition of specific iGDGTs. The $\delta^{13}C$ composition of iGDGT-3 is omitted because these measurements were only obtained for samples from AC. Samples with black borders have low purity scores (< 0.85) and are below 0.9 μg of sample material. While multiple $\delta^{13}C$ values were obtained for each sediment depth interval (sample), only one methane index value was calculated; thus the MI of the whole sample is plotted against the $\delta^{13}C$ values of each individual iGDGT compound from that sample. These plots mimic the analysis originally conducted by Zhang et al. (2011), which plots methane index against biphytane-b.

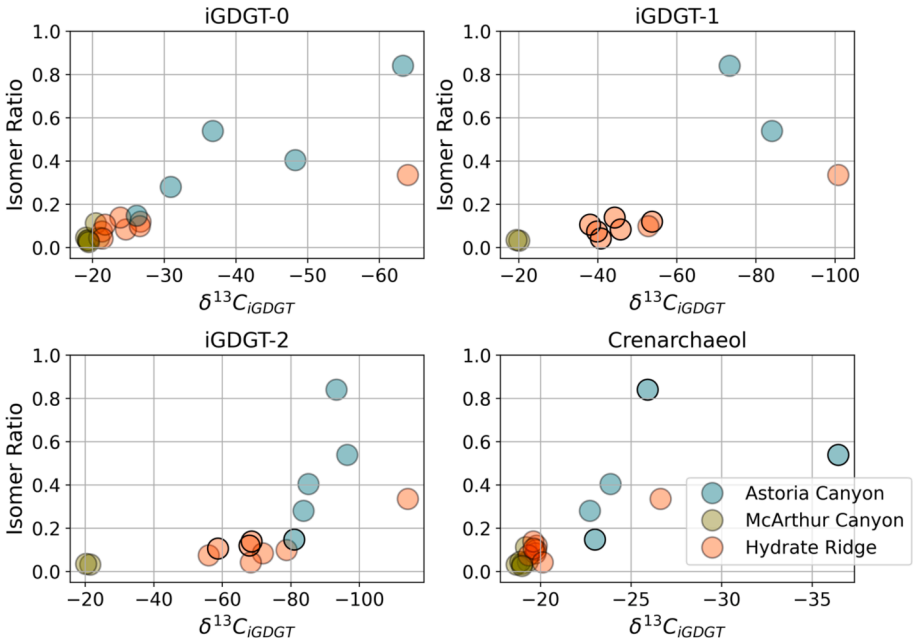

Fig. 4. The ratio between parallel and anti-parallel glycerol configurations relative to the $\delta^{13}C$ composition of specific iGDGTs. Higher ratios indicate a larger proportion of isomers in the anti-parallel configuration. The samples with black borders have low purity scores (< 0.85) and are below 0.9 μg of sample material. While multiple $\delta^{13}C$ values were obtained for each sediment depth interval (sample), only one isomer ratio value was calculated; thus the isomer ratio of the whole sample is plotted against the $\delta^{13}C$ values of each individual iGDGT compound from that sample, analogous to Fig. 3.

3.4. Bayesian mixing model

3.4.1. Bayesian modeling of endmember iGDGT contributions and $\delta^{13}C$ values

We used a Bayesian mixing model to ascertain the fractional contributions of distinct endmember sources to the iGDGT lipid pool, with the assumption of three types: planktonic (assumed 100% autotrophic), benthic methane-cycling, and benthic-non-methane cycling archaeal communities. In constructing the model, we implemented broad prior distributions based on existing literature; the upper and lower ranges of $\delta^{13}C$ values and lipid abundances used to set the model priors for the three endmembers are given in Table 2. We parameterized the benthic methane-cycling endmember to include both methanotrophic and methanogenic archaeal groups. The $\delta^{13}C$ range for this endmember (Table 2) was determined by considering the kinetic isotope fractionation imparted during methane oxidation and production. Prior $\delta^{13}C$ measurements of methane along Cascadia Margin are reported to range from *ca.* −60 to −40‰ (Pohlman et al., 2011; Joseph et al., 2013). Cell-specific or in-situ studies of methanotrophic archaea report up to 60‰ depletion in ^{13}C in archaeal lipids relative to source methane (Orphan et al., 2001; Stadnitskaia et al., 2008); similarly large fractionations have been observed during methane production (Penger et al., 2012). The distribution of lipid structures for the methane-cycling endmember includes observations from impacted sediments assumed to be dominated by methanotrophs (Zhang et al., 2011), and iGDGT distributions obtained from cultured archaeal methanogens (Bauersachs et al., 2015). For the planktonic endmember, the narrow range of $\delta^{13}C$ values is based on measurements obtained from suspended particulate matter in the water column (Hurley et al., 2019). The lipid distribution is based on reference lipid profiles from cold, pelagic marine environments, as outlined in Zhang et al. (2011). For the benthic non-methane-cycling endmember, the $\delta^{13}C$ range encompasses the presumed metabolisms of Benthic Marine Group D (MGD) and Miscellaneous Crenarchaeotal Group (MCG), which are thought to perform acetogenic and heterotrophic metabolisms although they have not yet been isolated from marine sediments (Lloyd et al., 2013; Baker et al., 2021). The lipid distributions are based on profiles of cultivated *Crenarchaeota*, with focus on known heterotrophic or facultatively heterotrophic taxa (Pearson et al., 2008).

Fig. 5 (top panel) shows the values of 94th percentile posterior distribution of the proportions of these endmembers comprising the total iGDGT pool for the three Cascadia locations. All three locations mainly

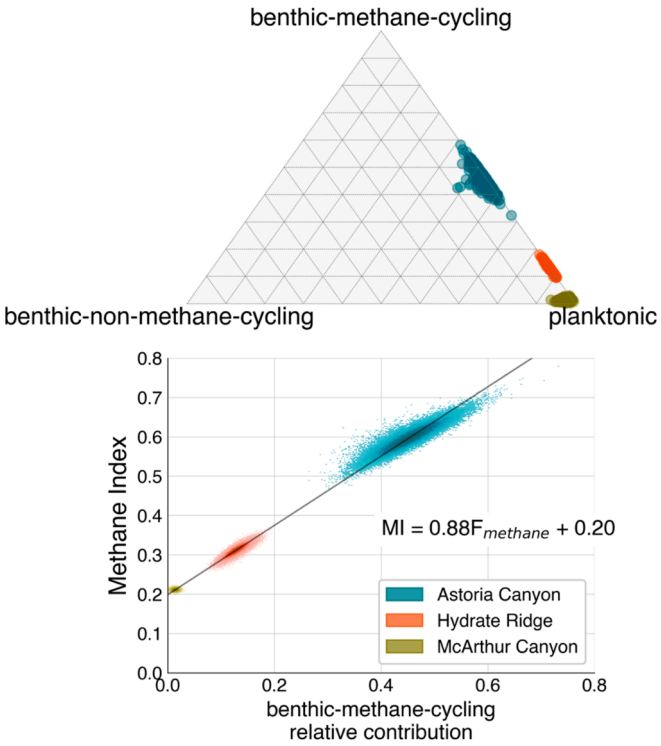

Fig. 5. Top. Posterior distributions of the relative proportions of planktonic, benthic methane-cycling, and non-methane cycling archaeal sources estimated using $\delta^{13}C$ and lipid distribution data for each sampling location. Bottom. Posterior estimates of MI values and inferred contributions of benthic-methane-cycling archaea for each location.

fall along a binary mixing line between the benthic-methane-cycling and planktonic endmembers, with minimal contributions from the benthic-non-methane cycling endmember. At AC, contributions from planktonic and benthic-methane-cycling endmembers are almost equal, with mean values of 0.54 and 0.45 respectively; the mean estimate for the benthic-non-methane-cycling contributions at AC is 0.01 (Fig. S2). At MC and HR, planktonic endmember contributions are dominant, with mean estimates of 0.97 and 0.87, respectively. The mean values for the benthic-methane-cycling endmember are 0.01 and 0.13 at MC and HR, and thus the benthic-non-methane-cycling endmember only contributes 0.02 at MC and < 0.01 at HR (Fig. S2).

The inferred mean methane index values for AC, HR, and MC are 0.60, 0.31, and 0.21 respectively (Fig. S3). The relationship between inferred benthic-methane-cycling contributions and observed methane index for each location shows a strong, positive linear relationship (Fig. 5, bottom panel). The positive intercept of 0.20 reflects the baseline MI value for sediments containing nearly zero benthic-methane-cycling contributions, assuming there are no other influencing factors on sedimentary iGDGT contributions. The linear fit provides a method to predict methane-cycling contributions based on MI values for systems mainly composed of benthic-methane-cycling and planktonic endmembers, i.e., those with near zero influence from other benthic or allochthonous communities.

Using these inferred relative iGDGT inputs, we generated a simulated chromatogram for each source (Fig. 6, Fig. S4). In this analysis, iGDGT-5 encompasses Cren' as well as other iGDGTs with m/z 1292, except for crenarchaeol itself. In the planktonic endmember, iGDGT-0 and crenarchaeol predominate, with smaller quantities of iGDGT-1, -2, and -5. Benthic methane-cycling sources, on the other hand, are characterized by abundant iGDGT-0 and -1, higher presence of iGDGT-2, and nearly complete absence of iGDGT-4, crenarchaeol, and iGDGT-5. The inferred relative iGDGT profile for the benthic-non-methane cycling endmember exhibits significant uncertainty in the posterior distributions and thus the simulated chromatogram. The inferred results show nearly uniform abundances of iGDGT-0, -1, -2, -3, -4, a small contribution of iGDGT-5, and minimal update of the prior distributions. The apparently near-zero contribution of crenarchaeol by benthic methane-cycling and non-methane-cycling endmembers is due to model parameterizations, where it is assumed that crenarchaeol is exclusively synthesized by planktonic sources (Table 2). Fig. S5 illustrates the difference between the prior and posterior distributions for the relative abundances of iGDGT in each source.

The inferred relative iGDGT profiles and fractional contributions are used to calculate mean predicted $\delta^{13}C$ values for each iGDGT (i.e., what would be recovered from hypothetical total sediments) at each location, and the mean $\delta^{13}C$ value for the three endmember sources (assumed to

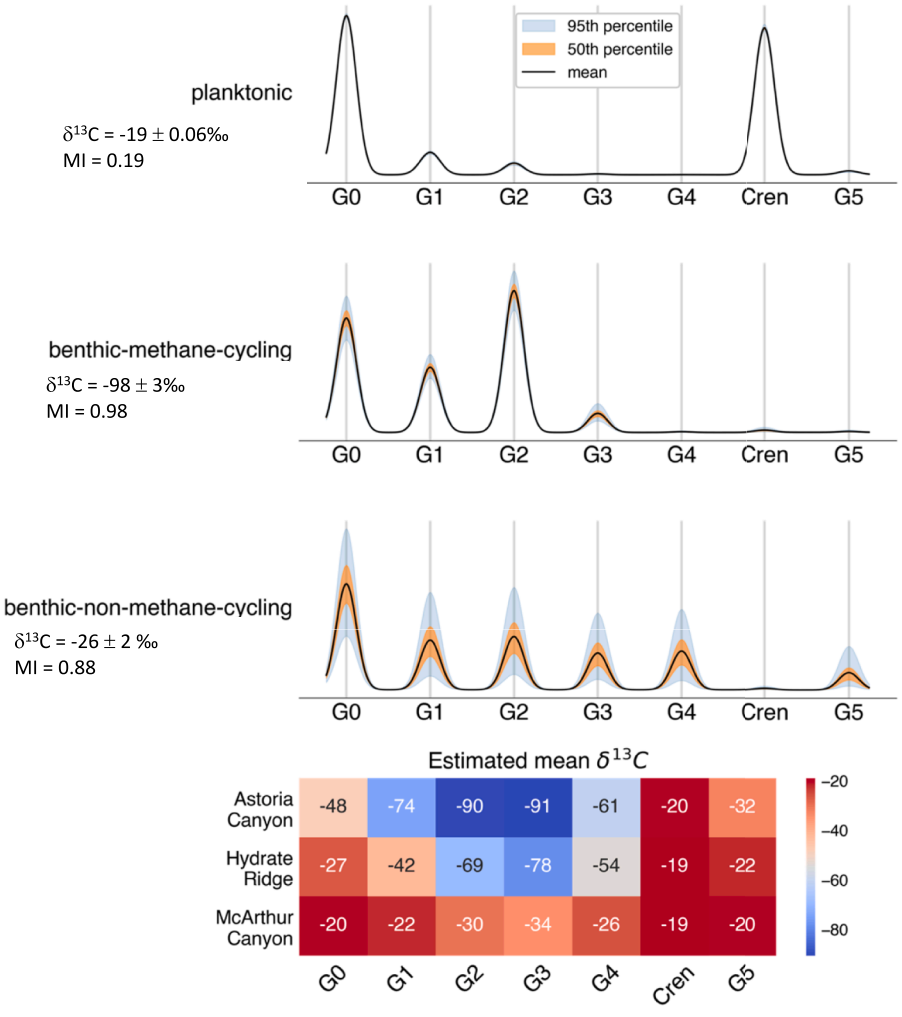

Fig. 6. Simulated chromatogram of estimated iGDGT profiles for each archaeal source; below the endmember title are the estimated mean $\delta^{13}C$ (94% HDI) and mean MI values for each endmember. The heatmap shows estimated mean $\delta^{13}C$ values for each iGDGT compound for each location, summarizing data across various sample depths and distances from the active methane plume.

be uniform throughout the Cascadia system; Fig. 6). The $\delta^{13}C$ estimate for the planktonic endmember is tightly constrained, with 94% highest density interval (HDI) between −19.1‰ and −18.8‰, and a mean value of −19.0‰ (Fig. S6). Benthic-methane-cycling and non-methane-cycling $\delta^{13}C$ posterior distributions are broader compared to their planktonic counterpart; the 94% HDI for the benthic-methane cycling ranges from −103.8‰ to −92.1‰ (mean value of –97.8‰) and between −29.9‰ and −22.4‰ (mean value of −26.1‰) for the benthic-non-methane cycling endmember. The minimal difference between the prior and posterior distributions of the benthic non-methane-cycling endmember is due to the limited observational signal associated with this source (i.e., ≤ 2% of the total iGDGT assemblage); thus the inferred mean $\delta^{13}C$ is the median of the prior distribution (Fig. S7).

Notably, the mixing model generates $\delta^{13}C$ estimates for iGDGTs for each endmember and cold-seep location that were not directly measurable due to insufficient sample material (Figs. S7 and S8). At AC, where methane-cycling sources account for nearly 50% of iGDGTs, the $\delta^{13}C$ values for iGDGT-0 are slightly ^{13}C-depleted (−48‰, see heatmap Fig. 6), indicating influence from both planktonic and benthic-methane-cycling sources. The estimates for iGDGT-1, -2, and -3 are significantly more negative, reflecting a larger methane-cycling influence, while the $\delta^{13}C$ value predicted for crenarchaeol in all three locations concurs with water-column measurements for planktonic iGDGTs (Hurley et al., 2019). The $\delta^{13}C$ value predicted for iGDGT-5 suggests a majority contribution from planktonic sources with minor input from methane-cycling sources. At HR and MC, the $\delta^{13}C$ estimates indicate dominance by planktonic endmembers, in agreement with the inferred source contributions. The small methane-cycling influence (13% relative contribution) at HR yields more ^{13}C-enriched estimates compared to AC, but still yields strongly negative $\delta^{13}C$ values for iGDGTs-1, -2, and -3. At MC, the $\delta^{13}C$ profiles strongly signal planktonic sources, with a slight depletion in ^{13}C for iGDGT-2 and -3 due to minor contributions from benthic-methane and non-methane cycling sources, estimated at about 3% of the total iGDGT lipid pool.

4. Discussion

4.1. Composition of archaeal endmembers

Diverse archaeal communities inhabit marine sediments, such as Bathyarchaeota (previously Miscellaneous Crenarchaeotal Group, MCG), Marine Benthic Group B and Group D, and lineages of Euryarchaeota; yet the majority are uncultured, and their biogeochemical niches, physiologies and metabolisms are not well characterized (Teske and Sørensen, 2008; Lloyd et al., 2011, 2013; Baker et al., 2021). In methane rich environments, such as Cascadia Margin, prior carbon isotopic investigations suggest that heterotrophic communities dominate the iGDGT assemblage (Biddle et al., 2006), while other lines of evidence instead suggest dominance by methane-cycling archaeal communities (Pancost et al., 2001; Liu et al., 2011). The distribution and abundances of benthic non-methane cycling archaea is largely unknown, and it remains contested whether these groups contribute appreciably to sedimentary lipid pool (Pearson and Ingalls, 2013; Besseling et al., 2018). Thus, determining the number and types of archaeal iGDGT sources and characterizing their composition has proven to be a challenge (Pearson et al., 2016; Zhu et al., 2021). Here, our Bayesian framework helps to quantify the relative contributions of multiple archaeal sources using $\delta^{13}C$ values of intact, core iGDGTs and their relative abundances.

Although cold-seep ecosystems are dense and varied in microbial life, our findings suggest that surface sedimentary iGDGTs are mainly contributed by planktonic and benthic-methane-cycling archaea. Importantly, we find that the planktonic signal is regionally consistent and stable, both isotopically and chromatographically, with the canonical compound crenarchaeol retaining its planktonic signature even in moderately methane-impacted areas such as HR. Our findings that sedimentary iGDGTs primarily originate from planktonic sources (>50% for all locations, even AC) agrees with earlier work (Pearson et al., 2016), which estimated that 2–38% of iGDGTs retrieved from marine sediments along the US continental margins have exogenous origins (i.e., are not planktonic). Biphytanes collected from surface sediments of Mediterranean cold seeps also were interpreted to contain substantial planktonic inputs, although the fractional contributions were not quantified (Pancost et al., 2001).

Significantly, we find that non-methane-cycling benthic archaea apparently account for a minimal fraction (≤2%) of the total iGDGTs at all studied locations. This result is surprising given that benthic non-methane cycling archaea are believed to comprise a significant portion of the subsurface biosphere (Teske and Sørensen, 2008). Our results suggest that these archaea either may not play a significant role in supporting the sediment ecosystems of shallow, continental-margin sediments; are too slow-growing to make a noticeable contribution to the iGDGT lipid pool; and/or are recycling relic planktonic material, making their $\delta^{13}C$ isotopic signature indistinguishable from that of planktonic sources (Biddle et al., 2006; Takano et al., 2010). This finding conflicts with other studies suggesting that benthic archaea, specifically heterotrophic archaea, are significant sources of iGDGTs (Biddle et al., 2006; Besseling et al., 2018; Zhu et al., 2021). The relative influence of this group on the sedimentary lipid pool may vary with respect to physiochemical conditions. Thus, more analyses should be conducted in other marine systems, including outside of continental margins and deeper in the sediment column.

The observed variation in benthic-methane-cycling contributions across the cold-seep sites likely stems from the dynamic and heterogenous nature of cold-seeps across space and time (Elvert et al., 2005). For example, differences in methane and/or sulfate availability or the oxygenation of surface sediments due to bioturbation by megafauna would locally inhibit anaerobic metabolism. Prior work has noted varying macrofaunal communities, methane fluxes, fluid flow and porewater characteristics across cold seep provinces (Elvert et al., 2005). Such dynamics could influence the growth rates of methane-cycling archaeal communities both temporally and geographically. For instance, MC samples primarily exhibit a planktonic signature despite being collected from areas of active methane release. This could imply a recent shift in the methane plume, not allowing enough time for methane-cycling communities to establish and contribute to the sedimentary iGDGT lipid pool. The predominantly planktonic signature at MC suggests that the methane flux currently is not substantially consumed by the archaeal community and is available to be oxidized by aerobic bacteria in the sediment or in the water column.

4.2. Inferred isotopic signatures and lipid profiles of endmembers

While the $\delta^{13}C$ signatures and lipid distributions can be determined for endmembers having representatives isolated in pure culture, the lipid characteristics of uncultured endmembers must be extrapolated from observations. Our Bayesian framework accommodates both cases, by simultaneously leveraging prior data and our new observations to yield robust $\delta^{13}C$ estimations for two of the three endmembers and their associated uncertainties. Due to insufficient data, our model does not provide improved $\delta^{13}C$ estimations for the non-benthic-methane cycling group (Fig. S7). The estimated mean $\delta^{13}C$ value (*ca.* –98‰; 94% HDI) for the benthic-methane-cycling endmember in the Cascadia region suggests that iGDGTs yielding similar $\delta^{13}C$ values predominantly originate from this source (e.g., iGDGTs-2 and -3 from AC). The two $\delta^{13}C$ values < −98‰ from HR are evidence that there is local heterogeneity to this endmember. Previous reports of $\delta^{13}C$ values of archaeal biphytanes and/or archaeol from methane-rich environments yield similar results to our observations and model inferences, including selected instances of values ≤ −100‰ (e.g., Hinrichs et al., 1999). Most observations, however, are modestly > −100‰; for example, $\delta^{13}C$ values between −90‰ and −80‰ were observed for biphytanes −b and −c (derivatives of

iGDGTs-1, -2, and -3) collected from mud volcanoes in the NE Atlantic (Stadnitskaia et al., 2008). Existing research on iGDGT distributions in methane-rich environments also reveals a significant overabundance of biphytane-b, which concurs with our estimated iGDGT distribution patterns (Pancost et al., 2001; Stadnitskaia et al., 2008; Liu et al., 2011; Zhang et al., 2011). Assuming a binary mixing system between planktonic and methane-cycling archaeal communities, our results indicate that benthic-methane cycling communities contribute *ca.* $\geq$ 90% of iGDGT-2 and -3 when MI values are $>$ *ca.* 0.5 and the fraction of the total iGDGT inventory contributed by the benthic-methane-cycling community is $>$ *ca.* 0.4 (Fig. 5).

Our inferred iGDGT profile for the local planktonic endmember is well-constrained and mirrors lipid profiles observed in cold, pelagic ocean settings, with high abundances of iGDGT-0 and crenarchaeol (Wuchter et al., 2006). Synthesis of crenarchaeol typically is thought to be performed exclusively by Nitrososphaerota, and its presence in marine settings may be an indicator of their ammonia-oxidizing physiology (Pitcher et al., 2011; Schouten et al., 2013). Our mean $\delta^{13}C$ estimates for the measured crenarchaeol across all three sites generally converge near −19‰. This aligns both with the modeled planktonic endmember value (–19.0‰, 94% HDI) and with previous $\delta^{13}C$ measurements of crenarchaeol (or its biphytane derivative) recovered from the water-column, US continental shelf, Mediterranean cold seeps, and NE Atlantic mud volcanoes (Pancost et al., 2001; Stadnitskaia et al., 2008; Pearson et al., 2016; Hurley et al., 2019). Thus, our results generally support the idea that crenarchaeol is robust biomarker for planktonic archaea. Importantly, the values of $\delta^{13}C < -20$‰ for crenarchaeol samples recovered at AC most likely result from co-elution of other compounds during HPLC, rather than benthic in-situ production. This is indicated by low purity scores for these samples. The NP-HPLC method used in this analysis does not resolve iGDGT-4, which elutes as a leading shoulder to crenarchaeol and cannot be baseline separated. Baseline separation is a requirement to avoid isotopic fractionation during chromatography, and thus co-eluting peaks cannot be split into separate fractions (Keller et al., 2023). Mass spectral analysis revealed a notable presence of iGDGT-4 in the AC samples having low purity scores; although iGDGT-4 constitutes only 1 to 2% of total iGDGTs, it represents a larger fraction within the crenarchaeol peak (*ca.* 5 to 15%).

The inferred mean $\delta^{13}C$ endmember value for benthic-non-methane cycling communities is −26.1‰; however, the 94% HDI for the posterior distribution closely mirrors the prior distribution, which was based on $\delta^{13}C$ values observed for biphytanes collected in the SMTZ of the Peru Margin and the $\delta^{13}C$ value of bulk total organic carbon measured in the Cascadia Margin region (Biddle et al., 2006; Pohlman et al., 2011). Similarly, the inferred estimates for the iGDGT lipid profiles (Fig. 6) also reflect the prior distributions. The priors were based on lipid profiles generated from cultivated *Crenarchaeota*, with emphasis on known heterotrophic or facultatively heterotrophic taxa (Table 2; Pearson et al., 2008). This could imply high confidence in the assumed profiles, but more likely the collected data do not provide a strong enough signal to influence the prior distributions, given the minimal inferred contributions from this endmember. More observations from samples with known benthic-non-methane cycling contributions will help to elucidate its lipid distribution pattern and isotopic signature.

4.3. Predicted methane index and impact on paleo-SST estimations

The methane index ratio is traditionally used to identify secondary influences that might affect paleo-SST estimations. MI traditionally is used as a binary indicator to distinguish between methane-impacted and non-methane-impacted sediments. The initial study by Zhang et al. (2011) established the relationship between the MI and observable ^{13}C depletion of archaeal biphytanes, assumed to reflect methane-cycling archaea. More recently, Kim and Zhang (2023) expanded on this work and determined a correlation between the MI and sedimentary methane fluxes using linear regression analysis. However, these studies do not provide a method to directly quantify iGDGT fractional contributions from methane sources and thus preclude a rigorous evaluation of the links between absolute MI values and *in situ* methane contributions. This has particular relevance to the choice of a "cut-off value" for diagnosing sediments impacted by methane cycling. Our study shows that the revised MI cut-off of 0.5 proposed by Kim and Zhang (2023) for sediments from non-polar regions would represent a major deviation from typical marine conditions, corresponding to $>$ 30% of the total iGDGT pool and likely the majority of iGDGT-2 and -3 derived from benthic methane-cycling sources. Despite clear cases of ^{13}C-depleted iGDGTs at HR (Fig. 3) the MI values at HR are *ca.* 0.3, generally interpreted as normal marine conditions (Zhang et al., 2011). We estimate that at a MI value of 0.3, there is a *ca.* $>$ 10% contribution from the benthic methane endmember. Thus, we determine the mean baseline MI value for pure planktonic endmembers to be 0.2, representing the zero-MI intercept in Fig. 5. While Zhang et al. (2011) reports the MI for normal marine conditions ranging from 0.03 to 0.3, our findings constrain this range–at least on the Cascadia Margin–to be from 0.17 to 0.20 (94% HDI, Fig. S9). The larger range previously proposed likely is due to the inclusion of polar samples, which push MI towards lower values.

We estimate that 88% of iGDGTs must originate from benthic-methane-cycling archaea to attain an MI value of 0.98, the inferred mean MI value for this endmember. This finding is consistent with the estimates provided by Kim and Zhang (2023). The influence of benthic non-methane-cycling (e.g., heterotrophic) archaea on the MI is ambiguous, primarily due to the scarcity of data. However, we speculate that deviations from the linear trend in Fig. 5 may indicate contributions from exogenous sources (benthic-non-methane or allochthonous endmembers), although additional data are required to substantiate this hypothesis.

A broadly positive relationship between the MI and anomalies in reconstructed SST (ΔSST; Fig. 7) signals that methane influence introduces positive bias into TEX_{86}-SST estimates, consistent with Zhang et al. (2011). The inferred mean TEX_{86} values for AC and HR (0.66 and 0.56, respectively; Figs. S10, S11) are significantly higher than the BAYSPAR predicted TEX_{86} value (mean 0.48) for Cascadia Margin based on the observed annual regional SST (*ca.* 13 °C, World Ocean Atlas 2018, Fig. 8). The nonlinear relationship between benthic methane-cycling contributions and inferred TEX_{86} values (Fig. 8) demonstrates that even small benthic methane cycling contributions (<15%) can yield positively biased TEX_{86} estimates, e.g., as seen for HR. The MI thus requires careful interpretation due to a non-proportional response in TEX_{86} to benthic-methane-cycling contributions (Fig. S12).

We binned the MI values into 0.1-unit intervals to assess the

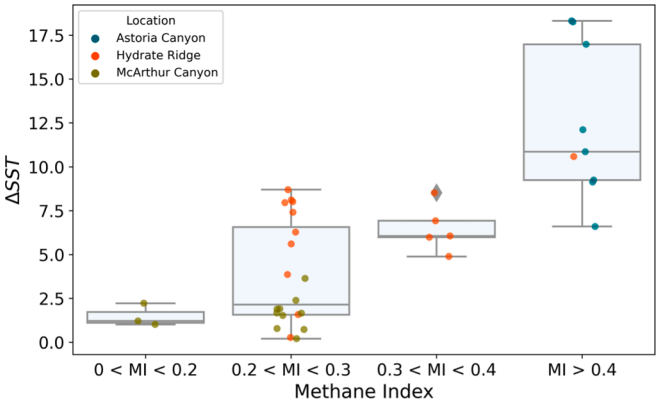

Fig. 7. Boxplot of the distribution of SST deviations (TEX_{86}-inferred minus *in situ* SST) across different MI intervals. Each box represents interquartile range (IQR) SST deviations, with the median highlighted by the black line. The boxplot extends to the lowest and highest values within 1.5 times the IQR from the quartiles, excluding the outlier from sample S39, which is marked with a diamond symbol.

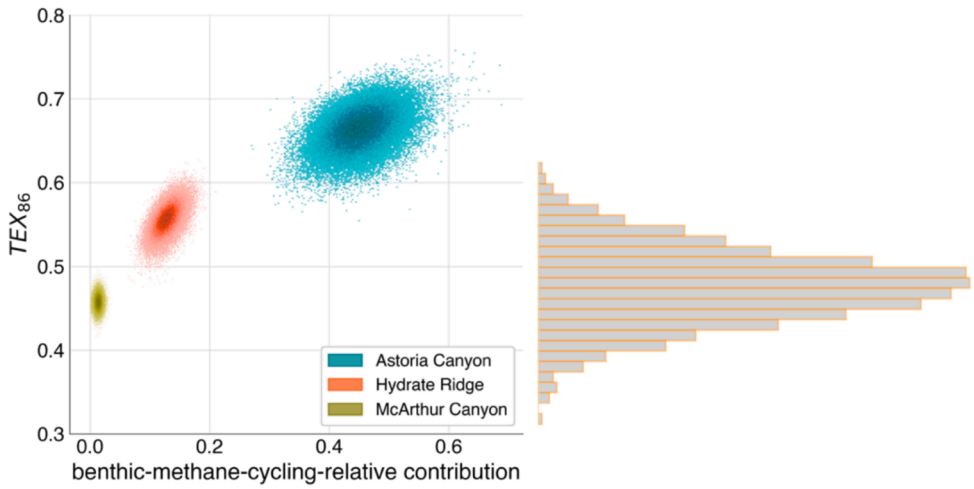

Fig. 8. Bivariate plot showing the relationship between posterior distributions for TEX_{86} ratios and benthic-methane-cycling contributions for each cold-seep location; the gray histogram shows the posterior distributions of the BAYSPAR TEX_{86} predictions calculated from average annual regional SST of *ca.* 13 °C (Tierney and Tingley, 2015; World Ocean Atlas, 2018).

associated distributions in ΔSST (Fig. 7, Table 3): MI < 0.2, 0.2 ≤ MI < 0.3, 0.3 ≤ MI < 0.4, and MI ≥ 0.4. Samples in the lower MI interval (< 0.2) yield ΔSST predictions within 2.5 °C of observed SSTs. Predicted SSTs for MI values between 0.2 and 0.3, denoting benthic contributions of *ca.* 1–11%, deviate by as much as 8.7 °C, although 95% confidence intervals for mean ΔSST are more constrained, ranging from 2.5 °C to 5.0 °C (Fig. 7). The next MI interval (0.3–0.4) yields a mean ΔSST value of 6.5 °C consistent with the greater methane contribution. In instances where the MI exceeds 0.4, representing benthic-methane-cycling contributions *ca.* > 20%, we estimate a mean ΔSST *ca.* 12.5 °C, with a 95% confidence interval between *ca.* 10 °C to 15 °C (Table 3). While our results echo previous research demonstrating that higher MI values positively bias paleo-SST estimates (Brien et al., 2017; Lattaud et al., 2021; He et al., 2022), our analysis demonstrates that some samples having MI < 0.4 generate > 5°C error in TEX_{86} and cannot reliably be identified during screening. Using the MI as a binary threshold-based indicator will thus be overly simplistic in some cases. We recommend the MI to be used to develop a correction-based approach or a refined error analysis for paleo-proxy reconstructions. Combining this metric with other complementary tools, such as compound-specific $\delta^{13}C$ analysis, may allow for better distinction of secondary iGDGT inputs at sites with suspected methane input.

4.4. Structural isomer configuration of methane-cycling archaea

To our knowledge, there currently are no published compound-specific $\delta^{13}C$ values for iGDGTs paired with selective *sn*2 ether cleavage products for those same compounds; this study presents the first analysis of this kind. Prior research has assessed glycerol configuration isomers found in shale samples known to have experienced methane cycling, finding a significant portion of iGDGTs in the anti-parallel configuration.

Table 3
Summary statistics of methane index intervals relative to Δ*SST* and percent error of TEX_{86}-SST estimates. The Δ*SST* metric represents the difference between TEX_{86}-derived SSTs and average annual regional SST of *ca.* 13 °C (World Ocean Atlas, 2018; see SI section 4 for more information).

MI interval	Mean Δ*SST*(°C)	95% CI mean Δ*SST*	Mean percent error	95% CI mean percent error
≤0.2	1.5	1.0–2.2	11.5	7.8–17.9
0.2–0.3	3.7	2.5–5.0	28.6	18.9–38.5
0.3–0.4	6.5	5.4–7.5	49.8	42.6–58.0
0.4–1.0	12.5	10.0–15.3	95.8	75.4–116.9

Our results agree with this pattern, showing that samples having a large contribution from the benthic-methane-cycling endmember, e.g., samples from AC, have a higher relative abundance of mpbm cleavage products (Fig. 4). Although the isomer analysis was performed on individual sediment depth horizons and not specific iGDGT compounds, we observe that the samples with lowest $\delta^{13}C$ values for iGDGT-2 and highest MI index values also exhibit the highest isomer ratios, indicating that the benthic-methane-cycling archaea are predominantly producing iGDGTs in the antiparallel configuration. Our findings also reveal a positive correlation between isomer ratio and ^{13}C-depletion (Fig. S13). The connection between isomer configuration and TEX_{86} still needs to be investigated.

Determining the underlying mechanisms that drive the synthesis of parallel versus anti-parallel iGDGTs falls outside the focus of this research. However, previous research has suggested that these isomers may be biological adaptations to temperature that influence membrane packing and fluidity (Sinninghe Damsté et al., 2018; Holzheimer et al., 2021). This is consistent with the idea that the full suite of isomeric forms of iGDGTs has evolved to confer distinct energetic and/or physiological advantages (Valentine, 2007). Synthesis of anti-parallel iGDGTs could represent an environmental adaptation, utilizing energetic properties of this glycerol configuration isomer to respond to energy stress. More research is needed in the future to understand the physiological role of iGDGT glycerol configuration isomers.

5. Conclusion

Applying a Bayesian framework to compound-specific $\delta^{13}C$ values of individual iGDGTs allowed us to robustly estimate the influence of methane-cycling archaea on the total sedimentary iGDGT assemblage. This approach also enabled inference of the iGDGT lipid profiles for the pure planktonic and methane-cycling archaeal endmembers. Our results indicate that the sedimentary iGDGT lipid pool in the cold-seep systems of the Cascadia Margin is predominantly influenced by these two endmembers, with minimal input from benthic-non-methane cycling (e.g., heterotrophic) archaea or other exogenous input. Such a limited third-component contribution provides little new insight into the enigmatic benthic archaea. We suggest applying the present framework to deeper pelagic systems to characterize this third endmember and evaluate its influence on TEX_{86} proxy ratios. The carbon isotopic signatures inferred here reinforce previous notions that crenarchaeol is a robust biomarker for *Nitrosphaerota* and that high relative abundance of iGDGT-2, coupled with a ^{13}C-depleted signature, strongly signifies methane impact. Cold-

seep environments with significant methane-cycling archaeal activity tend to have a greater proportion of iGDGTs in the anti-parallel glycerol configuration. Finally, we establish a quantitative relationship between benthic methane-cycling contributions and the MI ratio value, expanding on the works of Kim and Zhang (2023) and Zhang et al. (2011). We show that even samples with low MI values (e.g., < 0.4) can result in large TEX_{86}-derived SST errors. Complementary analyses, such as compound-specific isotopic analysis, should be used in tandem with the MI to better identify secondary inputs in sediments with suspected methane impact.

CRediT authorship contribution statement

Katherine J. Keller: Writing – review & editing, Writing – original draft, Visualization, Investigation, Formal analysis, Data curation, Conceptualization. **Mark M. Baum:** Writing - review & editing, Formal analysis, Visualization. **Xiao-Lei Liu:** Writing – review & editing, Methodology, Formal analysis. **Kemi Ashing-Giwa:** Writing – review & editing, Formal analysis. **Isabel R. Baker:** Writing – review & editing, Data curation. **Jerome Blewett:** Writing – review & editing, Formal analysis. **Ann Pearson:** Writing – review & editing, Writing – original draft, Supervision, Project administration, Investigation, Formal analysis, Conceptualization.

Declaration of competing interest

The authors declare that they have no known competing financial interests or personal relationships that could have appeared to influence the work reported in this paper.

Data availability

All data and code can be found in the linked Zenodo repository in the supplemental material.

Acknowledgements

We thank the anonymous reviewers for helpful feedback and comments. We thank Peter Girguis for samples, and Susan Carter and Samuel Phelps for lab assistance and helpful discussions. Funding was provided by Harvard University, the US National Science Foundation (award 1843285) and the American Chemical Society Petroleum Research Fund (ACS-PRF award 66614-ND2) to A.P., NASA Exobiology Program (80NSSC22K1559) to X.-L.L; J.B. acknowledges funding through an Agouron Foundation Geobiology Postdoctoral Fellowship.

Appendix A. Supplementary data

Supplementary data to this article can be found online at https://doi.org/10.1016/j.orggeochem.2024.104882.

References

Baker, B.J., Appler, K.E., Gong, X., 2021. New Microbial Biodiversity in Marine Sediments. Annual Review of Marine Science 13, 161–175.

Bauersachs, T., Weidenbach, K., Schmitz, R.A., Schwark, L., 2015. Distribution of glycerol ether lipids in halophilic, methanogenic and hyperthermophilic archaea. Organic Geochemistry 83–84, 101–108.

Besseling, M.A., Hopmans, E.C., Christine Boschman, R., Sinninghe Damsté, J.S., Villanueva, L., 2018. Benthic archaea as potential sources of tetraether membrane lipids in sediments across an oxygen minimum zone. Biogeosciences 15, 4047–4064.

Besseling, M.A., Hopmans, E.C., Bale, N.J., Schouten, S., Sinninghe Damsté, J.S., Villanueva, L., 2020. The absence of intact polar lipid-derived GDGTs in marine waters dominated by Marine Group II: Implications for lipid biosynthesis in Archaea. Scientific Reports 10, 1–10.

Biddle, J.F., Lipp, J.S., Lever, M.A., Lloyd, K.G., Sørensen, K.B., Anderson, R., Fredricks, H.F., Elvert, M., Kelly, T.J., Schrag, D.P., Sogin, M.L., Brenchley, J.E., Teske, A., House, C.H., Hinrichs, K.-U., 2006. Heterotrophic Archaea dominate sedimentary subsurface ecosystems off Peru. Proceedings of the National Academy of Sciences of the United States of America 103, 3846–3851.

Blewett, J., Elling, F.J., Naafs, B.D.A., Kattein, L., Evans, T.W., Lauretano, V., Gallego-Sala, A.V., Pancost, R.D., Pearson, A., 2022. Metabolic and ecological controls on the stable carbon isotopic composition of archaeal (isoGDGT and BDGT) and bacterial (brGDGT) lipids in wetlands and lignites. Geochimica et Cosmochimica Acta 320, 1–25.

Brien, C.L.O., Robinson, S.A., Pancost, R.D., Sinninghe Damsté, J.S., Schouten, S., Lunt, D.J., Alsenz, H., Bornemann, A., Bottini, C., Brassell, S.C., Farnsworth, A., Forster, A., Huber, B.T., Inglis, G.N., Jenkyns, H.C., Linnert, C., Littler, K., Markwick, P., Mcanena, A., Mutterlose, J., Naafs, B.D.A., Püttmann, W., Sluijs, A., van Helmond, N.A.G.M., Vellekoop, J., Wagner, T., Wrobel, N.E., 2017. Earth-science reviews cretaceous sea-surface temperature evolution : constraints from TEX 86 and planktonic foraminiferal oxygen isotopes. Earth-Science Reviews 172, 224–247.

Elling, F.J., Gottschalk, J., Doeana, K.D., Kusch, S., Hurley, S.J., Pearson, A., 2019. Archaeal lipid biomarker constraints on the Paleocene-Eocene carbon isotope excursion. Nature Communications 10, 1–10.

Elvert, M., Hopmans, E.C., Treude, T., Boetius, A., Suess, E., 2005. Spatial variations of methanotrophic consortia at cold methane seeps: Implications from a high-resolution molecular and isotopic approach. Geobiology 3, 195–209.

He, J., Jia, J., Guo, W., Jia, G., 2022. Archaeal tetraether lipids and their biphytane carbon isotope composition in sediments along an estuarine biogeochemical gradient. Geochimica et Cosmochimica Acta 318, 452–467.

Hinrichs, K.-U., Hayes, J.M., Sylva, S.P., Brewer, P.G., DeLong, E.F., 1999. Methane-consuming archaebacteria in marine sediments. Nature 398, 802–805.

Ho, S.L., Laepple, T., 2016. Flat meridional temperature gradient in the early Eocene in the subsurface rather than surface ocean. Nature Geoscience 9, 606–610.

Holzheimer, M., Sinninghe Damsté, J.S., Schouten, S., Havenith, R.W.A., Cunha, A.V., Minnaard, A.J., 2021. Total synthesis of the alleged structure of crenarchaeol enables structure revision. Angewandte Chemistry 60, 17504–17513.

Huguet, C., Hopmans, E.C., Febo-Ayala, W., Thompson, D.H., Sinninghe Damsté, J.S., Schouten, S., 2006. An improved method to determine the absolute abundance of glycerol dibiphytanyl glycerol tetraether lipids. Organic Geochemistry 37, 1036–1041.

Hurley, S.J., Close, H.G., Elling, F.J., Jasper, C.E., Gospodinova, K., McNichol, A.P., Pearson, A., 2019. CO_2-dependent carbon isotope fractionation in Archaea, Part II: the marine water column. Geochimica et Cosmochimica Acta 261, 383–395.

Ingalls, A.E., Shah, S.R., Hansman, R.L., Aluwihare, L.I., Santos, G.M., Druffel, E.R.M., Pearson, A., 2006. Quantifying archaeal community autotrophy in the mesopelagic ocean usinq natural radiocarbon. Proceedings of the National Academy of Sciences of the United States of America 103, 6442–6447.

Jenkyns, H.C., Schouten-Huibers, L., Schouten, S., Sinninghe Damsté, J.S., 2012. Warm Middle Jurassic-Early Cretaceous high-latitude sea-surface temperatures from the Southern Ocean. Climate of the Past 8, 215–226.

Joseph, C., Campbell, K.A., Torres, M.E., Martin, R.A., Pohlman, J.W., Riedel, M., Rose, K., 2013. Methane-derived authigenic carbonates from modern and paleoseeps on the Cascadia margin: Mechanisms of formation and diagenetic signals. Palaeogeography, Palaeoclimatology, Palaeoecology 390, 52–67.

Keller, K.J., Phelps, S.R., Pearson, A., 2023. Evaluation of iGDGT carbon isotope fractionation in high performance liquid chromatography. Organic Geochemistry 176, 104526.

Kellermann, M.Y., Wegener, G., Elvert, M., Yoshinaga, M.Y., Lin, Y.S., Holler, T., Mollar, X.P., Knittel, K., Hinrichs, K.-U., 2012. Autotrophy as a predominant mode of carbon fixation in anaerobic methane-oxidizing microbial communities. PNAS 109, 19321–19326.

Kim, B., Zhang, Y.G., 2023. Methane Index: Towards a quantitative archaeal lipid biomarker proxy for reconstructing sedimentary methane fluxes. Geochimica et Cosmochimica Acta 354, 77–87.

Könneke, M., Bernhard, A.E., de la Torre, J.R., Walker, C.B., Waterbury, J.B., Stahl, D.A., 2005. Isolation of an autotrophic ammonia-oxidizing marine archaeon. Nature 437, 543–546.

Lattaud, J., De Jonge, C., Pearson, A., Elling, F.J., Eglinton, T.I., 2021. Microbial lipid signatures in Arctic deltaic sediments–Insights into methane cycling and climate variability. Organic Geochemistry 157, 104242.

Liu, X., Lipp, J.S., Hinrichs, K.-U., 2011. Distribution of intact and core GDGTs in marine sediments. Organic Geochemistry 42, 368–375.

Lincoln, S.A., Wai, B., Eppley, J.M., Church, M.J., Summons, R.E., Delong, F., 2014. Planktonic Euryarchaeota are a significant source of archaeal tetraether lipids in the ocean. PNAS 111, 9858–9864.

Liu, X., Lipp, J.S., Birgel, D., Summons, R.E., Hinrichs, K.-U., 2018. Organic geochemistry predominance of parallel glycerol arrangement in archaeal tetraethers from marine sediments: structural features revealed from degradation products. Organic Geochemistry 115, 12–23.

Liu, X., Russell, D.A., Bonfio, C., Summons, R.E., 2019. Organic Geochemistry Glycerol configurations of environmental GDGTs investigated using a selective *sn*2 ether cleavage protocol. Organic Geochemistry 128, 57–62.

Lloyd, K.G., Alperin, M.J., Teske, A., 2011. Environmental evidence for net methane production and oxidation in putative ANaerobic MEthanotrophic (ANME) archaea. Environmental Microbiology 13, 2548–2564.

Lloyd, K.G., Schreiber, L., Petersen, D.G., Kjeldsen, K.U., Lever, M.A., Steen, A.D., Stepanauskas, R., Richter, M., Kleindienst, S., Lenk, S., Schramm, A., Jørgensen, B.B., 2013. Predominant archaea in marine sediments degrade detrital proteins. Nature 496, 215–218.

Orphan, V.J., House, C.H., Hinrichs, K.-U., McKeegan, K.D., DeLong, E.F., 2001. Methane-consuming archaea revealed by directly coupled isotopic and phylogenetic analysis. Science 293, 484–487.

Pancost, R.D., Hopmans, E.C., Sinninghe Damsté, J.S., 2001. Archaeal lipids in mediterranean cold seeps: Molecular proxies for anaerobic methane oxidation. Geochimica et Cosmochimica Acta 65, 1611–1627.
Pearson, A., Hurley, S.J., Walter, S.R.S., Kusch, S., Lichtin, S., Zhang, Y.G., 2016. Stable carbon isotope ratios of intact GDGTs indicate heterogeneous sources to marine sediments. Geochimica et Cosmochimica Acta 181, 18–35.
Pearson, A., Ingalls, A.E., 2013. Assessing the use of archaeal lipids as marine environmental proxies. Annual Review of Earth and Planetary Sciences 41, 359–384.
Pearson, A., Pi, Y., Zhao, W., Li, W., LI, Y., Inkseep, W., Perevalova, A., Romanek, C., Li, S., Zhang, C.L., 2008. Factors controlling the distribution of archaeal tetraehters in terrestrial hot springs. Applied and environmental microbiology 74, 3523–3532.
Penger, J., Conrad, R., Blaser, M., 2012. Stable carbon isotope fractionation by methylotrophic methanogenic archaea. Applied and Environmental Microbiology 78, 7596–7602.
Pitcher, A., Wuchter, C., Siedenberg, K., Schouten, S., Sinninghe Damsté, J.S., 2011. Crenarchaeol tracks winter blooms of ammonia-oxidizing Thaumarchaeota in the coastal North Sea. Limnology and Oceanography 56, 2308–2318.
Pohlman, J.W., Bauer, J.E., Waite, W.F., Osburn, C.L., Chapman, N.R., 2011. Methane hydrate-bearing seeps as a source of aged dissolved organic carbon to the oceans. Nature Geoscience 4, 37–41.
Polik, C.A., Elling, F.J., Pearson, A., 2018. Impacts of paleoecology on the TEX_{86} sea surface temperature proxy in the Pliocene-Pleistocene Mediterranean Sea. Paleoceanography and Paleoclimatology 33, 1472–1489.
Rattanasriampaipong, R., Zhang, Y.G., Pearson, A., Hedlund, B.P., Zhang, S., 2022. Archaeal lipids trace ecology and evolution of marine ammonia-oxidizing archaea. PNAS 119, e2123193119.
Schouten, S., Hopmans, E.C., Sinninghe Damsté, J.S., 2013. The organic geochemistry of glycerol dialkyl glycerol tetraether lipids: A review. Organic Geochemistry 54, 19–61.
Shah, S.R., Mollenhauer, G., Ohkouchi, N., Eglinton, T.I., Pearson, A., 2008. Origins of archaeal tetraether lipids in sediments: Insights from radiocarbon analysis. Geochimica et Cosmochimica Acta 72, 4577–4594.
Sinninghe Damsté, J.S., Rijpstra, W.I.C., Hopmans, E.C., Uijl, M.J.D., Weijers, J.W.H., Schouten, S., 2018. The enigmatic structure of the crenarchaeol isomer. Organic Geochemistry 124, 22–28.
Stadnitskaia, A., Ivanov, M.K., Sinninghe Damsté, J.S., 2008. Application of lipid biomarkers to detect sources of organic matter in mud volcano deposits and post-eruptional methanotrophic processes in the Gulf of Cadiz, NE Atlantic. Marine Geology 255, 1–14.
Takano, Y., Chikaraishi, Y., Ogawa, N.O., Nomaki, H., Morono, Y., Inagaki, F., Kitazato, H., Hinrichs, K.-U., Ohkouchi, N., 2010. Sedimentary membrane lipids recycled by deep-sea benthic archaea. Nature Geoscience 3, 858–861.
Taylor, K.W.R., Huber, M., Hollis, C.J., Hernandez-Sanchez, M.T., Pancost, R.D., 2013. Re-evaluating modern and Palaeogene GDGT distributions: Implications for SST reconstructions. Global and Planetary Change 108, 158–174.
Teske, A., Sørensen, K.B., 2008. Uncultured archaea in deep marine subsurface sediments: Have we caught them all? The ISME Journal 2, 3–18.
Tierney, J.E., 2014. Biomarker-based inferences of past climate: the TEX86 Paleotemperature Proxy. Treatise on. Geochemistry 12, 379–393.
Tierney, J.E., Tingley, M.P., 2015. A TEX_{86} surface sediment database and extended Bayesian calibration. Scientific Data 2, 1–10.
Valentine, D.L., 2007. Adaptations to energy stress dictate the ecology and evolution of the Archaea. Nature Reviews Microbiology 5, 316–323.
Wuchter, C., Schouten, S., Wakeham, S.G., Sinninghe Damsté, J.S., 2006. Archaeal tetraether membrane lipid fluxes in the northeastern Pacific and the Arabian Sea: Implications for TEX_{86} paleothermometry. Paleoceanography 21, 1–9.
Yoshinaga, M.Y., Lazar, C.S., Elvert, M., Lin, Y.S., Zhu, C., Heuer, V.B., Teske, A., Hinrichs, K.-U., 2015. Possible roles of uncultured archaea in carbon cycling in methane-seep sediments. Geochimica et Cosmochimica Acta 164, 35–52.
Zhang, Y.G., Zhang, C.L., Liu, X.L., Li, L., Hinrichs, K.-U., Noakes, J.E., 2011. Methane Index: A tetraether archaeal lipid biomarker indicator for detecting the instability of marine gas hydrates. Earth and Planetary Science Letters 307, 525–534.
Zhang, Y.G., Pagani, M., Wang, Z., 2016. Ring Index: A new strategy to evaluate the integrity of TEX86 paleothermometry. Paleoceanography 31, 220–232.
Zhu, Q.Z., Elvert, M., Meador, T.B., Becker, K.W., Heuer, V.B., Hinrichs, K.-U., 2021. Stable carbon isotopic compositions of archaeal lipids constrain terrestrial, planktonic, and benthic sources in marine sediments. Geochimica et Cosmochimica Acta 307, 319–337.